JOURNAL OF AEROSPACE COMPUTING, INFORMATION, AND COMMUNICATION
Vol. 2, August 2005

Detection of Digital Elevation Model Errors Using X-band Weather Radar

Steven D. Young*
National Aeronautics and Space Administration, Hampton, Virginia 23681

and
Maarten Uijt de Haag†
Ohio University, Athens, Ohio 45701

Flight in Instrument Meteorological Conditions requires pilots to manipulate flight controls while referring to a Primary Flight Display. The Primary Flight Display indicates aircraft attitude along with, in some cases, many other state variables such as altitude, speed, and guidance cues. Synthetic Vision Systems have been proposed that overlay the traditional information provided on Primary Flight Displays onto a scene depicting the location of terrain and other geo-spatial features. Terrain models used by these displays must have sufficient quality to avoid providing misleading information. This paper describes how X-band radar measurements can be used as part of a monitor, and/or maintenance system, to quantify the integrity of terrain models that are used by systems such as Synthetic Vision. Terrain shadowing effects, as seen by the radar, are compared in a statistical manner against estimated shadow feature elements extracted from the stored terrain model from the perspective of the airborne observer. A test statistic is defined that enables detection of errors as small as the range resolution of the radar. Experimental results obtained from two aircraft platforms hosting certified commercial-off-the-shelf X-band radars test the premise and illustrate its potential.

I. Introduction

The purpose of this study is to investigate the feasibility of using certified X-band weather radar (WxR) and its standard data bus and data outputs as part of a monitoring function that provides an improved level of integrity for a Digital Elevation Model (DEM). DEM integrity is quantified by the probability that errors larger than a predefined value are detected by the monitor function. The predefined value is selected based on the amount of error that is acceptable during a particular flight operation with respect to safety. DEM integrity is a component of overall system integrity. In general, system integrity can be defined as the probability that the system will provide timely warnings when it should not be used for its intended function. When using a DEM as part of a flight deck display, the probability of providing misleading terrain information will contribute to system-level integrity.

In this section, a review of the motivation, WxR technology, and DEM semantics is provided. To appreciate the results of this study, a basic understanding of airborne radar,[1] the Global Positioning System (GPS),[2] an Inertial Reference Unit (IRU),[3] and a DEM,[4] is recommended.

Received 21 September 2004; revision received 21 January 2005; accepted for publication 7 July 2005.
* Aerospace Technologist, Langley Research Center, 1 South Wright Street, steven.d.young@nasa.gov, AIAA Senior Member, and Member of the AIAA Digital Avionics Technical Committee.
† Assistant Professor, Department of Electrical and Computer Engineering, 329 Stocker Center. uijtdeha@ohiou.edu

A. Motivation

Flight in low visibility conditions requires pilots to manipulate flight controls while referring to a Primary Flight Display (PFD). The PFD indicates aircraft attitude along with, in some cases, many other state variables such as altitude, speed, and guidance cues in the form of Flight Director (FD) symbology. The FD is a predictor that indicates to pilots where to steer the aircraft. A conventional PFD provides no information about the terrain environment in the vicinity of the aircraft. In low visibility conditions, terrain avoidance is accomplished by using the FD to follow a well-designed flight path, referencing a chart, and/or monitoring and communicating with Air Traffic Control. Furthermore, a Terrain Awareness and Warning System (TAWS) may provide warnings of terrain proximity.[5] While TAWS has improved aviation safety tremendously, the Federal Aviation Administration has deemed TAWS products "advisory-only" primarily due to the fact that the DEMs used by TAWS do not have proven integrity.

Synthetic Vision Systems (SVS) have been proposed that overlay the traditional information provided by PFDs onto a scene depicting the location of terrain and other geo-spatial features.[6] Because of the compelling nature of an SVS PFD function, it is expected that pilots will use all of the information presented as navigational aids, particularly when there is little or no visibility. This leads to a fundamental question. How can an SVS PFD function be designed such that pilots can have confidence that the picture is not lying to them? In terms of avionics systems engineering, this question translates to a problem of reducing the likelihood of providing misleading information to flight crews to an acceptably low level. A quantitative approach to this integrity problem is likely required to enable certification of an SVS PFD function.

An important assumption with respect to this integrity problem should be stated. It is assumed that overlaying high integrity PFD-like functions, such as FD guidance, on top of lower integrity data, such as terrain, will result in lower system integrity than a traditional PFD. When information with different qualities is presented on a display, there will be cases where the information may conflict. An extreme example would be when errors result in FD guidance intersecting the virtual depiction of terrain. Although these errors could be detected automatically by a well-designed SVS, less obvious situations may occur in which the guidance may be perceived by pilots as too close to terrain (e.g. too low or too high). Although pilots may be trained to trust the high integrity guidance, the display may be considered misleading when/if these situations occur. Without the terrain depiction, the presumed high integrity guidance would be followed without question. This assumption, along with the fact that there may be cases where FD guidance is unavailable has helped motivate the research.

B. Digital Elevation Models

DEMs are spatial representations of the geographic feature commonly known as terrain. Terrain is defined for aviation purposes as "the natural surface of the earth excluding obstacles".[7] Traditionally, DEMs are stored as grids with fixed intervals between the grid points. Grid points are spatially referenced using prescribed horizontal and vertical datums. Latitude-Longitude-Height coordinates relative to a geodetic reference frame are most commonly used for DEMs.

DEM errors can be classified as systematic error, random error, and blunders.[7] Systematic error is a low-frequency spatial error that affects a set of observations in the same way over a geographic region. Common examples of systematic error are bias, rotation, and scale factor. These errors usually result from imprecise calibration of the measurement sensor. Other more malicious and subtle systematic errors include: reversing latitude/longitude coordinates, misordering the elevation values with respect to the expected convention, interpolating between discrete measurement points, down-sampling artifacts, unit conversion errors, and incorrect datum assumptions.

Random errors, also known as noise, refer to the basic inherent property that estimates of a random variable rarely agree with its expectation. These errors usually show high frequency spatial behavior, and are described by a probability density function (PDF) along with parameters of the PDF such as the variance or standard deviation.

Blunders are observations that cannot be considered as belonging to the PDF. These errors include outliers that may have been introduced during data collection or during data processing. Blunders also include data omissions. Omissions in DEMs are often referred to as voids. These voids are areas where the data collection sensor was unable to measure the terrain elevation.

With respect to existing DEMs, only an estimate of the amount of random error to expect is usually provided with the data set. For example, consider DEMs provided according to the Digital Terrain Elevation Data (DTED™) Level 1 file specification.[8] These DEMs will include 1,442,401 elevation estimates covering one degree of latitude by one

degree of longitude spaced regularly at intervals of three arc-seconds. Per the specification, elevation estimate errors within DTED™ Level 1 files should not exceed an absolute horizontal accuracy of 50 m with 90% circular error probability with respect to the reference ellipsoid, and an absolute vertical accuracy of 30 m with a 90% linear error probability with respect to Mean Sea Level (MSL).[8] In addition, with respect to the SVS operational objectives, it is important to recognize that although the stated quality of a DEM may be sufficient in terms of accuracy, there is no associated integrity that can be expected or derived from this metric alone. As described in Section I-A, integrity depends on the operational use of the data.

C. X-band Weather Radar

In today's aircraft fleet, a frequently-used range measurement sensor is the WxR. These X-band pulsed-doppler radars are used primarily to provide flight crews with a display of weather information and to provide a forward-looking wind-shear detection capability. A secondary purpose, as described in Ref. 9, is "ground-mapping to facilitate navigation by display of significant land contours". Although using the WxR display to aid navigation has been historically a pilot-specific talent derived from extensive use of the device, recent work has shown that integration with DEMs can supplement on-board navigation systems and detect ground-based hazards.[10,11]

A typical certified WxR system includes a Receiver/Transmitter (R/T), an antenna, an antenna pedestal, an indicator/display, and a control unit. The WxR system is designed such that all signal processing is performed by the R/T and data products are provided to the display. The control unit allows an operator to configure the radar settings such as range, tilt angle, and mode. A Rockwell-Collins WxR-2100[12] was used for testing of the concepts presented in this paper.

Details on the characteristics of commercial certified WxR systems can be found in Ref. 13. Operating frequencies for X-band systems range from 9.3 to 9.5 GHz. Antenna diameters vary from 15 to 30 inches with gains ranging from 28.9 to 35 dB, respectively. Beam-width can vary from 2.9° to 6.0°. Antennas scan up to ±90° with respect to the longitudinal axis of the aircraft at a specified rate of 45°/sec. Range can be set by the pilot to 5, 10, 20, 40, 80, 160, or 320 nmi; however, the number of range bins with reported reflectivity measurements remains fixed at 512. Each reflectivity measurement is quantized into four levels with a fifth used for severe windshear. For display, colors are associated with these levels for each range bin during scanning. Measurement interval time is approximately 6 ms using a 0.25° azimuth resolution during scanning. The above specifications are taken from Ref. 9 and therefore, are not applicable to all X-band radars.

D. Related Work

In Ref. 14 a technology is described which uses a WxR to detect terrain and obstacles and alert the pilot in a timely manner. This technology is strictly a sensing function and as such, does not perform the required DEM integrity monitoring function. A more closely related technology is described in Ref. 11; this technology suggests a terrain database verification capability using a WxR sensor that interleaves weather measurements with terrain measurements. A test statistic is defined as the fraction of radar measurements that cannot be explained by other on-board data sources—including a terrain model. The Autonomous Precision Approach and Landing System (APALS™) technology described in Ref. 10 was designed to enable precision approaches using stored geo-spatial data and WxR measurements. APALS™accomplishes this by providing position fixes for the navigation system during final approach.

The operational concept for the proposed monitor is based largely upon the work described in Refs. 15 and 16 where DEM integrity is monitored and thus established using a downward-looking radar altimeter (DLRA). The DLRA monitor proposed in Refs. 15 and 16 uses consecutive radar altimeter and GPS position measurements to synthesize a terrain profile. The synthesized profile is then compared to the profile obtained from the DEM at the same locations. Differences are assessed statistically with respect to expected behavior and to requirements for probability of false alarm, P_{FA}, and probability of missed detection, P_{MD}. P_{MD} is the nomenclature used by the DLRA to indicate the DEM integrity value ($1 - P_{MD}$). The DLRA monitor has been shown to be an effective method of establishing integrity for DEMs.[16] However, the DLRA concept does have limitations due to the nadir measurement domain and assessments pertain to terrain that has already been over-flown.

II. Operational Concept

Building upon the DLRA approach, the proposed monitor seeks to detect failures using independent range measurements to terrain features and comparing them to expected values derived using GPS position solutions, attitude information, and a DEM. The operational concept presented here is focused on detection. Isolating the source of failures will be the subject of follow-on work. To overcome limitations of DLRA monitoring, the proposed monitor uses a forward-looking sensor, namely the WxR. By using forward-looking range measurements, both vertical and horizontal errors should become observable, and therefore, an improved detection capability is expected. Additionally, there is an operational advantage to using this approach. For TAWS and SVS displays, the potential hazards will be out-in-front of the pilot. By establishing integrity using measurements ahead of the aircraft's position, the pilot should have time to take action in the presence of compromised integrity.

The monitor would act as an intermediary between the source data and the SVS or TAWS displays checking any data requested by the display software against independent source(s). When a statistically significant difference is observed among the independent source(s), the pilot could be informed that the integrity of the displayed information is in question. When differences are not observed, the pilot can be assured that the display is operating at its specified performance level. The monitor concept assumes that the probability of displaying misleading terrain information when using the monitor would be much less than when not using the monitor, thereby, increasing overall system integrity. Additionally, differences could be logged and checked later as part of DEM maintenance and update procedures.

As previously mentioned, to observe errors that may ultimately result in misleading terrain information, measurements of terrain features are required from a source that is independent of the DEM. Although the primary function of the WxR is to measure moisture-related weather, the radar will also receive echoes from the ground if terrain is within the coverage of its antenna.

Operationally, the proposed monitor function attempts to extract terrain features from the WxR data bus without modifying the radar equipment. Only minimal configuration changes (e.g. range, scan limits) may be required from its normal operational mode. No ground components such as reflectors at surveyed locations are required. Further, in order to keep the sensor measurements independent from DEM-derived synthetic measurements, the terrain database is not used to determine where to point the radar. While this expectation-driven DEM-predictive approach can be used to achieve integrity, a higher level of integrity can be achieved by keeping the two completely independent.

III. Terrain Feature Extraction

Previously, the authors have presented an approach to achieving DEM integrity for SVS by implementing a monitor.[16–20] The monitor includes an algorithm that consists of two parallel threads. Each thread consists of a Shadow Detection and Extraction (SHADE) function that extracts terrain-related shadow features from independent sources and translates them into a common reference domain.[20] This enables disparity checking to determine statistical agreement. The two threads will be discussed separately. For more details, see Ref. 20.

A. Terrain Feature Extraction From Ground-Mapping Radar

The WxR-based thread extracts terrain-related features from measurements provided by the WxR. Each radar scan, S, consists of N radial measurements, each at a different azimuth pointing direction, α_i, where $i = 1, \ldots, N$. Furthermore, each radial measurement consists of M range bins, or intervals, with a corresponding value that represents the magnitude of the energy seen by the radar in that range interval.

Range bins are identified by an integer number, j, and a range bin size, ΔR. The range interval covered by a range bin is $(j-1)\cdot\Delta R < R < j\cdot\Delta R$. Measurements for each WxR scan can be represented by the set given in (1), where $\sigma^W_{i,j}$ represents the range bin value reported for a particular radial and range bin. One WxR scan therefore represents a set of NM measurements.

$$S = \{\sigma^W_{i,j} | i = 1, \ldots, N;\ j = 1, \ldots, M\} \tag{1}$$

Radars conforming to the standard interface[9] quantize the value, $\sigma^W_{i,j}$, into an integer in the range (0.3) and report the value for $M = 512$ range bins.[9]

For the current implementation, the terrain features of interest are shadowed regions. These features are identified as those segments along each radial where all of the range bin values equal zero, indicating a reflected energy value below the noise floor of the radar. Range bins whose values are non-zero, before and after these segments, are identified as shadow edges. To improve confidence in the shadow detection, a feature is only classified as a shadow feature if both a front and back edge is detected, or if a shadow with a front edge extends to the range setting of the radar.

Mathematically, the result, H_i^W, of the WxR shadow detection thread for each radial measurement i can be represented as (2) by applying a three-state finite state machine (FSM) to the $\sigma_{i,j}^W$ values.[20]

$$H_i^W = \{\eta_{i,j}^W = FSM(\sigma_{i,j}^W) | i = 1, \ldots, N;\ j = 1, \ldots, M\} \tag{2}$$

Ternary shadow state values are assigned as follows. "$\eta_{i,j}^W = -3$" is assigned when a radial measurement begins with a series of zero's. For these range bins, the algorithm cannot discern whether the range bin is shadowed or not. "$\eta_{i,j}^W = 1$" is assigned when the range bin value is greater than zero and therefore is not shadowed. "$\eta_{i,j}^W = 0$" is assigned when the range bin value is zero and is assumed to be shadowed.

B. Terrain Feature Extraction From a Digital Elevation Model

Whereas the WxR shadow detection thread can produce results directly from the WxR measurements, the DEM-based thread requires a model of the WxR measurement mechanism.[20] The model assumes that when energy hits terrain that has any surface component facing the antenna, a portion of the energy will be reflected back to the antenna resulting in non-zero reflectivity values in the corresponding range bins. However, for regions of terrain that are hidden from the perspective of the antenna (i.e. not in line-of-sight), little or no energy will be reflected and zero reflectivity values can be expected for the corresponding range bins.

To apply the model, the proposed algorithm uses (i) aircraft position (latitude, L^G, longitude, λ^G, and height, h^G) determined from GPS receiver measurements, (ii) aircraft attitude (pitch, θ, roll, ϕ, and heading, ψ) from an IRU, (iii) the antenna pointing direction (azimuth, α, and tilt, γ) from the WxR, (iv) a beam model, and (v) a DEM. Because traditional ray tracing approaches require excessive computational cycles that make implementation problematic, an alterative method has been implemented that uses depression angle as the basis for determining the shadow locations.[20] In this case, depression angle is defined as the angle from the antenna down to a point on the DEM.

Computed depression angles are compared to the expected range of angles that encompass the main beam for a particular measurement. Based on an assumed shadow model, the range of angles where the strongest WxR reflectivity estimates are expected would be within the three-dB beam-width, θ^B. This range of angles, $\phi^{d\,min,0}$ to $\phi^{d\,max,0}$, is γ_i minus/plus $\theta^B/2$. The result of the DEM-based thread for each radial measurement i can be represented by (3) using a four-state FSM.

$$H_i^D = \{\eta_{i,j}^D = FSM(\phi_{i,j}^d) | i = 1, \ldots, M\} \tag{3}$$

Shadow state values are assigned as follows. "$\eta_{i,j}^D = -3$" is the initial state and is assigned when the depression angle is outside the antenna beam model mentioned above. "$\eta_{i,j}^D = 1$" is assigned when the depression angle is inside the range of the antenna beam model and therefore the range bin is not shadowed. "$\eta_{i,j}^D = 2$" is assigned when the depression angle is a local maxima inside range of antenna beam model and therefore the range bin represents the location of a shadow leading edge. "$\eta_{i,j}^D = 0$" is assigned after local maxima and until the depression angle becomes greater than local maxima; these range bins are assumed to be shadowed.[20]

IV. Disparity Checking

Disparity checking comprises the final stage of the monitor function and consists of computing a consistency measure and comparing this measure to a pre-defined threshold. If the threshold is exceeded during the flight, terrain database integrity may be compromised. Operationally, it is recommended that pilots are alerted when this condition exists and that these events are logged to support maintenance and update procedures. The following sections describe the statistical basis for choosing a consistency metric, the method for computing values for this metric, and the method for establishing appropriate thresholds.

A. Theoretical Foundation

As previously discussed, SHADE produces feature vectors (H^W, H^D) that represent terrain shadow environments that are derived from two independent sources. SHADE produces these vectors in the same reference domain; therefore, ideally, differences should be zero as the sensor scans the terrain environment. However, due to random error components that exist with the data sources, statistically valid inferences with respect to agreement cannot be drawn from individual point comparisons. Specifically, we know that the WxR, the GPS receiver, the IRU, and the DEM will provide data that includes a random error component. These errors will be manifest as disparities (i.e. differences) in the products of the two threads of SHADE. The monitoring approach assumes that a prescribed amount of disparity is acceptable for a particular operation. This leads to the null hypothesis given by (4).

$$H_0\text{: } f_D \sim N(0, \sigma_D) \tag{4}$$

H_0 denotes that the fault-free behavior is characterized by disparities that are Normally distributed with zero mean and a standard deviation, σ_D. Alternate hypotheses can be stated for faulty behaviors. For example, (5) provides an alternate hypothesis representing the presence of a bias error in the disparities, μ_D.

$$H_1\text{: } f_D \sim N(\mu_D, \sigma_D) \tag{5}$$

Additional alternate hypotheses can be generated for other types of errors, however, this discussion focuses on the detection of bias-like errors. H_0 and H_1 assume that a Normal PDF can represent the true PDF. Given H_0 and H_1 the challenge becomes determining σ_D, the standard deviation for disparity in the fault-free state.

Several disparity metrics can be defined using the SHADE outputs. For this paper, shadow feature disparity, D_k, is given by (6) and is found on a per-radial basis using the shadow center range bin number, C_k. For either thread, the center range bin number is found using (7) where F_k and B_k are the front and back edge range bin numbers, respectively. Edge locations are determined by looking at the transitions from/to non-zero reflectivity values to/from zero reflectivity values. For example, if $H_i^W = \{-3, -3, 1, 1, 0, 0, 0, 1\}$, then the shadow center range bin number is six. Shadow front and back edge range bin numbers are four and eight, respectively.

$$D_k = C_k^W - C_k^D \tag{6}$$

$$C_k = \frac{F_k + B_k}{2} \tag{7}$$

From Ref. 21, the mean, μ_D, and variance, σ_D^2, for this disparity is given by (8) and (9). Further, as long as C_k^W and C_k^D are independent, the covariance will be zero and the PDF of D can be found by convolving the corresponding PDFs.[21]

$$\mu_D = \mu_{C^W} - \mu_{C^D} \tag{8}$$

$$\sigma_D^2 = \sigma_{C^W}^2 + \sigma_{C^D}^2 - 2\text{cov}(C^W, C^D) \tag{9}$$

If we assume that errors in F and B are independent and have zero-mean Normal distributions with variances of σ_F^2 and σ_B^2, respectively, then we arrive at a PDF for disparity, D, given by (10) that is consistent with our null hypothesis given by (4). In other words, for our null hypothesis to hold, errors in the front and back shadow edge range bin numbers generated by the two threads of the monitor must be independent and distributed as zero-mean Normal PDFs.

$$f_D \sim N(0, \sigma_D) \tag{10}$$

B. Establishing a Test-statistic for Disparity

Based on the expected error distributions for the results produced by both threads of SHADE, a metric for quantitatively assessing disparity can be postulated. Previous work suggests the mean-square difference of disparity as an appropriate metric.[15,16] The ratio of the number of features seen by the radar to the number of features seen by any means has been also suggested as a metric.[11]

In this paper an alternate test statistic is chosen. Instead of squaring the disparity and finding the mean over a series of samples,[15] the mean of the disparity is computed first and then scaled and squared. This will cause the monitor to be more sensitive to bias-like low-frequency errors per our hypotheses and less sensitive to random high-frequency errors. Specifically, a test statistic, T, is defined as (11) where N_D is the number of measurements used to establish the disparity test-statistic and D is found using (6). The scaling of D to create $\tilde{D}$ in (12) results in a zero-mean Normal PDF with unit variance.

$$T = \tilde{D}^2 = \left\{ \frac{1}{N_D} \sum_{x=1}^{N_D} \tilde{D} \right\}^2 \tag{11}$$

$$\tilde{D}_x = \left(\frac{1}{\hat{\sigma}_D} \right) D_x \tag{12}$$

It follows that the PDF for T will be a chi-squared distribution with one degree-of-freedom and a non-centrality parameter, λ_{NCP}, of zero. This PDF is given by (13) and (14). The mean, μ_T, and variance, σ_T^2, of T will be one and two, respectively.

$$f_T \sim \chi^2(1, 0) \tag{13}$$

$$f_T(u) = \frac{u^{-1/2} e^{-u/2}}{\sqrt{2}\sqrt{\pi}} \tag{14}$$

Recall the discussion of hypothesis testing with respect to the disparity metric, D. The corresponding null and alternate hypotheses using T are given by (15) and (16).

$$H_0\text{: } f_T \sim \chi^2(1, 0) \tag{15}$$

$$H_0\text{: } f_T \sim \chi^2(1, \lambda_{NCP}) \tag{16}$$

To determine the PDF of T, two assumptions are made: (i) the error PDFs for C^D and C^W are Normal with zero mean and standard deviations of σ_{C^D} and σ_{C^W}, respectively; (ii) C^D and C^W are independent random variables. The first assumption follows from the earlier assumption for the PDF of errors in F and B. The second assumption is based on the fact that C^D and C^W are generated from independent sources of information.

Based on the derivation above, a detection threshold, T_D, appropriate for any user-selected P_{FA} can be found using (17) where $f_T(u)$ is the PDF of T given in (14).

$$1 - P_{FA} = \int_0^{T_D} f_T(u) du \tag{17}$$

The selection of P_{MD} bounds the integrity of the monitor. For example, setting P_{MD} to 10^{-5} will guarantee that as long as the measured T is less than T_D, integrity is 1–10^{-5} or better. P_{MD} will also determine a lower bound on the magnitude of error that can be detected by the monitor at this integrity level. To illustrate, consider Fig. 1. The black curve is the expected distribution of T in the fault-free case. When unexpected bias errors occur, the chi-squared distribution will become a non-central chi-squared distribution with a non-centrality parameter, λ_{NCP}. Three such cases are shown in Fig. 1. Note how the unexpected bias errors create a hump in the PDF of various magnitudes.

Figure 1 illustrates the trade-off between P_{FA}, P_{MD}, and the detectable bias. Recall that P_{MD} is the area under the non-central PDF from zero to the detection threshold. The amount of bias in disparity that is required to push up the PDF until the area equals the desired P_{MD} represents the minimum amount of bias error that can be detected with the desired integrity. The relationship between $\mu_{\min}$ and λ_{NCP} is given by (18).

$$\mu_{\min} = \sigma_D \sqrt{\lambda_{NCP}} \tag{18}$$

Table 1 provides the detection threshold, T_D, the non-centrality parameter, λ_{NCP}, and $\mu_{\min}$ for example user-defined configurations. Units for σ_D and $\mu_{\min}$ are range bins. Table 1 illustrates again the trade-off between false

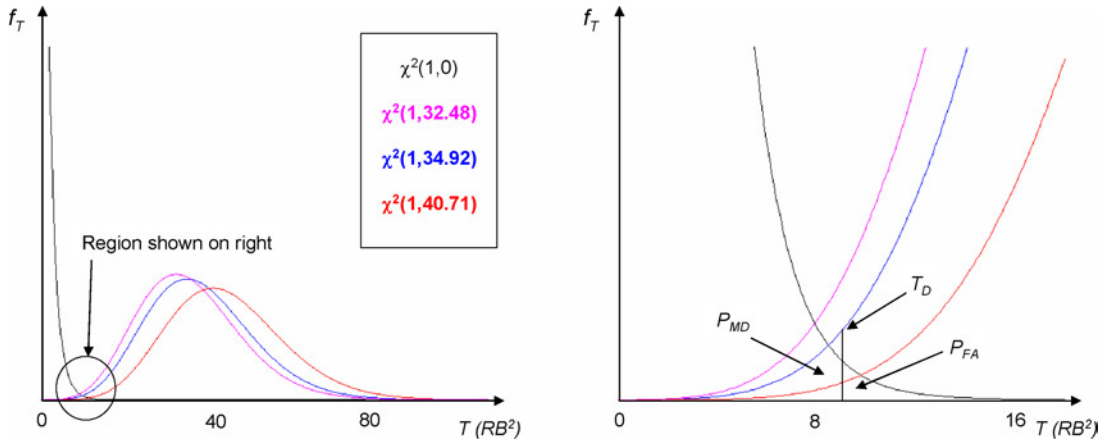

Fig. 1 Test statistic PDF in fault-free and faulty cases.

Table 1 Sample monitor configurations.

σ_D	P_{FA}	P_{MD}	λ_{NCP}	$\mu_{\min}$	T_D
1	10^{-1}	10^{-5}	34.92	5.91	2.71
	10^{-3}	10^{-3}	40.71	6.38	10.83
	10^{-5}	10^{-1}	32.48	5.70	19.51
2	10^{-1}	10^{-5}	34.92	11.82	2.71
	10^{-3}	10^{-3}	40.71	12.76	10.83
	10^{-5}	10^{-1}	32.48	11.40	19.51

alarms and missed detections. When the detection threshold is lowered, more false alarms can be expected, however, there will be fewer missed detections and, therefore, a higher level of integrity. Also, as we increase the acceptable amount of disagreement by increasing σ_D, we will lose fidelity in our detection capability—$\mu_{\min}$ will increase.

Note. The examples given in Table 1 apply to detection of shadow center point disparity bias. Appropriate thresholds for hypotheses representing other failure classes can also be derived.

C. Consideration

For each radial, there are four possible scenarios facing the disparity checker: (i) both threads detect a shadow, (ii) neither thread detects a shadow, (iii) only the WxR-based thread detects a shadow, and (iv) only the DEM-based thread detects a shadow. Computing disparity for scenario (i) has been discussed and is found using (6). Disparity for scenario (ii) is assumed to be zero. For scenarios (iii) and (iv) a penalty function is defined that assigns a disparity value based on the proximity and size of the shadow detected by the single thread. A penalty function can be used that is based on the following heuristics: larger shadows should incur a larger penalty and closer shadows should incur a larger penalty. Experimental data has shown that even in the presence of large DEM errors, cases where only one thread sees a shadow occur infrequently and the majority of these are small noise-like shadows.

V. Testing Platforms

The proposed functionality has been tested using data acquired on two platforms: a McDonnell-Douglas DC-8 (Figure 2) and a Gulfstream G-V (Figure 3). The DC-8 flights were flown from July 28 through August 4, 2003 originating at Edwards Air Force Base, Edwards, CA. Test trajectories were flown over an area near Modesto, CA.[19] The G-V flights occurred July 8 to July 24, 2004 in the vicinity of the Reno-Tahoe International Airport (RNO) in Reno, NV.[22] The WxR for the both tests was a WxR-2100 manufactured by Rockwell-Collins.[12] On the G-V, the focal plane array antenna size had to be reduced to fit in the confines of a smaller radome; this constrained azimuth

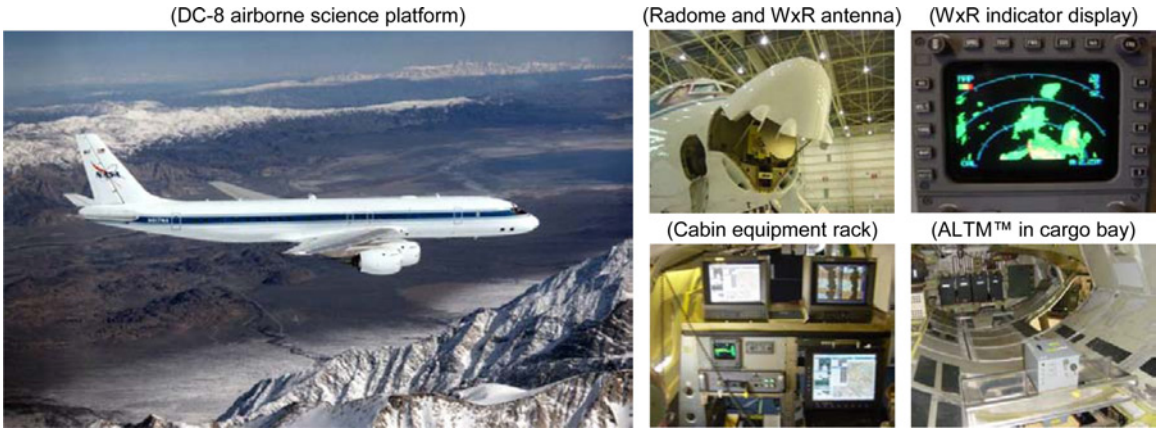

Fig. 2 DC-8 test aircraft and equipment installations.

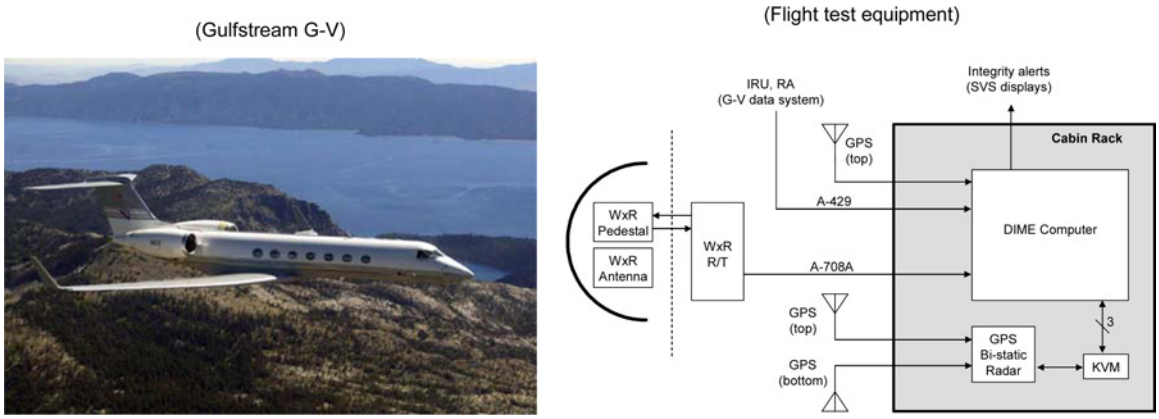

Fig. 3 G-V test aircraft and equipment installations.

scanning to ±48°. Each aircraft had a unique IRU. During the testing, a data processing computer synchronized and recorded all data while also hosting a Novatel GPS receiver.

Position solutions were corrected using the Wide Area Augmentation System. Interface to the WxR was via the standard data bus.[9] A total of 73 approaches were flown by the G-V at RNO. The test aircraft and equipment are shown in Figs. 2 and 3.

VI. Experimental Results

A. SHADE WxR-derived Product Calibration

For the WxR thread of SHADE, shadow edge locations are determined by looking at the transitions from/to non-zero reflectivity values to/from zero reflectivity values[23] provides a detailed discussion of the effects of terrain shadowing on radar sensitivity. The PDF for surface reflectivity is constrained by minimum and maximum measured clutter (signal) strength. Because the noise floor and saturation ceiling can be range dependent, the PDF may be constrained by the strongest noise level and the minimum saturation strength. This causes probability mass to be folded into the area surrounding the mean. Somewhere between these bounds will be the actual PDF limits for a particular set of measurements. Further, the PDF will be affected by changing amounts of noise, shadow, and saturation that depend on spatial coverage (i.e. a non-stationary random variable).

To avoid this non-deterministic shortcoming, theoretical discussions of radar clutter PDFs tend to use clutter-only patches. Because SHADE is looking for boundaries between clutter and noise, the PDFs derived in texts such as,[23–25]

do not directly apply. In fact, it appears that PDFs for these boundaries have not been derived previously. For these reasons, WxR calibration is suggested as a method of empirically deriving the characteristic performance of radar with respect to terrain-related features such as shadowing. This procedure can also be used to test assumptions of Normality.

Data collected by the DC-8 has been used to compare WxR-derived shadow edge locations to reference shadow edge locations over a region of moderate terrain. Reference edge locations were established using the DEM-derived thread of SHADE along with a high-quality DEM and kinematically-derived position and attitude solutions.

A reference DEM was generated for a region near Modesto, CA. Terrain elevations are stored in this DEM as a grid with five meter post-spacing and a vertical accuracy less than one meter (1σ). The reference DEM represents over 44 million elevation points. The data required to generate this DEM was collected using an Airborne Laser Terrain Mapping (ALTM) system.[26]

Ranging error for ALTM is a function of the pulse rise time and signal-to-noise ratio and is on the order of 2–5 cm (1σ). ALTM scan angle errors have been estimated at 0.0007° (1σ). ALTM IRU attitude errors have been estimated as 0.008° (1σ) for pitch and roll, and 0.015° (1σ) for heading. Kinematic GPS positioning errors have been estimated as 5–15 cm (1σ).[27] ALTM processing tools use data collected from the entire sensor suite to produce a DEM with a vertical accuracy of 15–30 cm (1σ) for all elevation values. Vertical accuracy for ALTM systems is determined by flying calibration segments over surveyed control points.

Now that a reference DEM has been produced, a reference trajectory for the aircraft flight path during WxR operation is required. This reference trajectory is produced using GPS and IRU data collected by ALTM, as well as GPS base station data collected by a continuously operating reference station.[28] By using the PosPac toolset from Applanix,[29] a Smoothed Best-Estimate Trajectory (SBET) can be generated. This SBET provides position and attitude for the flight at 50 Hz and synchronized to GPS time. A specific flight maneuver to be used for the WxR calibration was planned for the DC-8. This maneuver was designed to bi-sect the ALTM DEM coverage so that $\pm 45^\circ$ of WxR scanning, to a range of 10 nmi, would be included. Vertically, the aircraft remained less than 1000 ft AGL. After processing the data, the SBET root-mean-square position error was found to be <3 cm; while the attitude errors were found to be less than 140 μdeg. These accuracies are more than sufficient for the SBET to be used as reference trajectory information for the calibration.

For this test, the radar was configured to provide data per[9] using six bit encoding of the reflectivity values over 256 range bins and out to 20 nmi. This resulted in an effective range bin size of 144.8 m. The antenna scanned in azimuth over a $\pm 90^\circ$ sector at an average rate of 40°/sec. Radial measurements were produced every 0.5° during scanning.

Although physically the antenna is continuously scanning in both directions, the WxR-2100 provides data that updates in one direction, from -90° to $+90^\circ$, repeatedly. The WxR, stabilized to remain local-level, accumulates and processes the raw data to produce this desired effect for the pilot's radar indicator. Finally, and most importantly, all radar data received from the radar was stored along with a GPS-referenced timestamp to enable synchronization during the analysis with position and attitude data that were logged separately.

At this point, as long as we use enough independent samples, all of the required information is available to observe the distribution of errors for shadow edges as seen by the WxR. The data set consisted of 40 WxR scans covering the $\pm 45^\circ$ sector in front of the aircraft during the low-level WxR calibration maneuver. The 40 scans encompassed 7.5 minutes of flight. Two representative scans are shown in Fig. 4; the black areas are the range bins with associated values equal to zero, whereas the non-black areas represent the non-zero valued range bins.

SHADE is applied to the measurements; the WxR thread extracts shadows seen by the radar, and the DEM-derived thread extracts shadows observed using our reference DEM and SBET. The result of the latter is our truth-reference for shadow features that should be seen by the WxR during the calibration maneuver. The residual difference of these two (measurement—reference) is the expected shadow feature error for the radar. For example, Fig. 5 shows the shadow center point residuals and the distribution of these residuals using a range constraint of five nmi. The resulting estimate for σ_{C^W} is 3.01 range bins. The residual distribution shown in Fig. 5 is rejected by the Kolmogorov-Smirnov test for Normality. This indicates that over-bounding of the tails with a Normal (Gaussian) distribution may be required to support the Normality assumptions previously stated in (4) and (10). Over-bounding methods have previously been investigated during development of integrity monitors for the Local Area Augmentation System (LAAS).[30] Similar methods could be applied here.

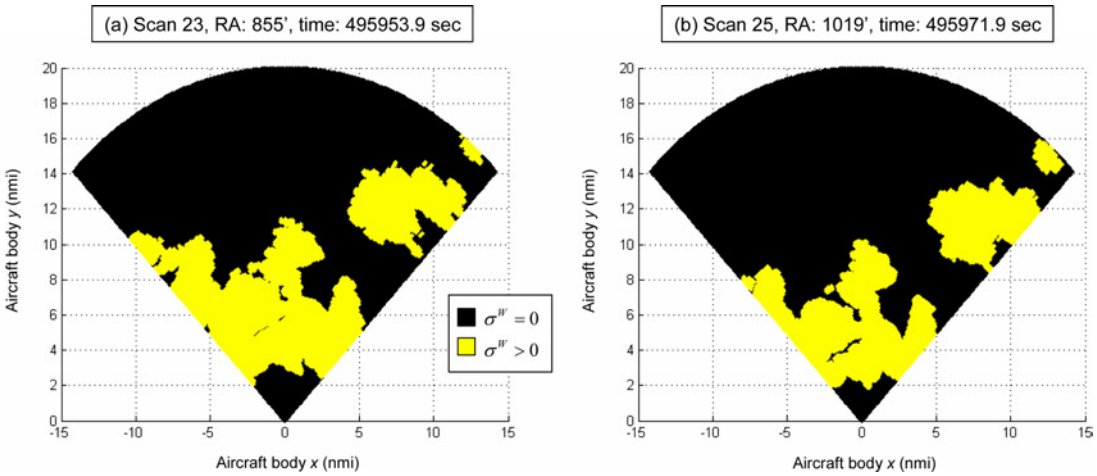

Fig. 4 Selected WxR scans during calibration maneuver.

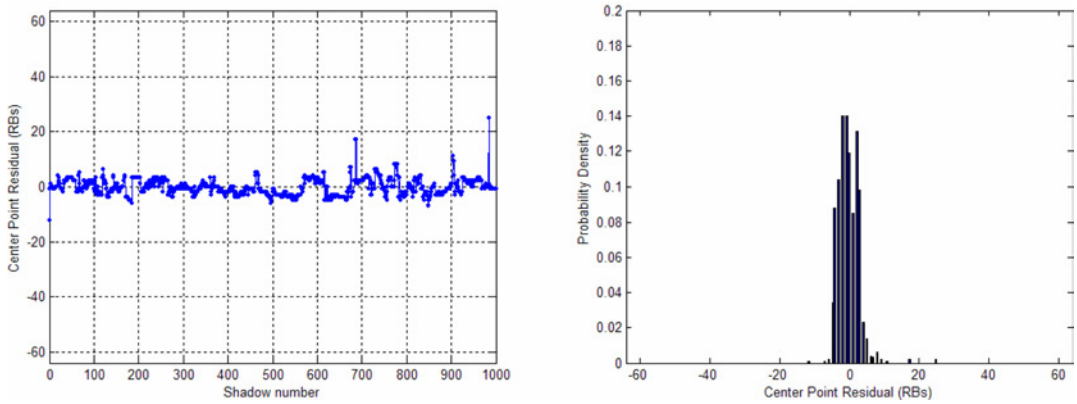

Fig. 5 WxR shadow feature center point residuals ($R = 5$ nmi).

B. SHADE DEM-derived Product Calibration

To estimate the expected distribution of shadow feature errors produced by the DEM-derived thread of SHADE in the fault-free state, a reference DEM is used to represent the true height of the terrain at each post location. In addition, reference aircraft state information is specified. Monte Carlo simulation trials are then executed wherein SHADE produces corrupted outputs resulting from input data randomly chosen from the expected error distributions of the systems providing the inputs. Expected error distributions for source data can come from equipment data sheets for avionics and from metadata files provided by the data provider for DEMs. An example calibration using the Monte Carlo method follows.

The reference database is a one arc-second (∼23 m) DEM centered at RNO. The coverage area is 100 nmi × 100 nmi. The average elevation for this DEM is 1720 m MSL. Minimum and maximum elevations for the DEM are 1149 and 3280 m MSL, respectively. The standard deviation of the elevations is about 73 m. Reference aircraft state information is given in Table 2 including assumed error PDFs. The error PDFs were chosen based on typical operational performance of the systems providing the input data to the DEM-derived thread of SHADE.

Monte Carlo simulation trials are generated at specified altitudes and at 360 azimuthal pointing directions. For each trial, SHADE input data is chosen from the Normal distributions given in Table 2. 256 range bins of size of 144.8 m are assumed. Range is limited to 10 nmi and only the first shadow detected along each radial is considered. Figure 6 illustrates the distribution of residuals for the shadow feature center points at an aircraft altitude of 2000 m MSL.

Table 2 Reference aircraft state information and assumed error distributions.

Parameter	Reference value	Error PDF
Latitude	39.49917°	N(0, 20 μdeg)
Longitude	−119.76750°	N(0, 20 μdeg)
Altitude	Varies	N(0, 5 m)
Pitch	0.0°	N(0, 0.01°)
Roll	0.0°	N(0, 0.01°)
Heading	0.0°	N(0, 0.01°)
Azimuth (WxR)	[0.359°]	N(0, 0.01°)
Tilt (WxR)	0.0°	N(0, 0.01°)

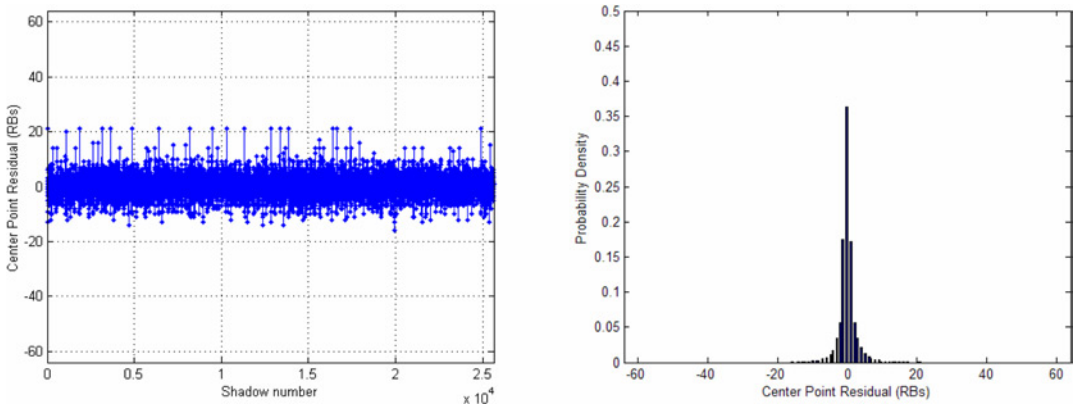

Fig. 6 DEM shadow feature center point residuals ($R = 10$ nmi).

As with the WxR thread calibration, this distribution is rejected by the Kolmogorov-Smirnov test for Normality. As such, over-bounding methods such as the ones suggested in Ref. 30 must be applied to meet any associated Normality assumptions.

Table 3 provides the mean and standard deviations of the residuals (i.e. errors) at various altitudes resulting from the Monte Carlo trials. These numbers were generated using a fixed range of 10 nmi and a minimum shadow size of three range bins and a maximum shadow size of 126 range bins. As expected, altitude relative to terrain has a significant impact on the perceived shadow environment.

Note. The distribution of errors for the products of SHADE will be physically constrained (i.e. discretized) by the radar interface.[9] For example, when using a five nmi range limit and a minimum shadow size of three range bins, the domain of F will be integers in the range *(1.60)*, while the domain of B will be integers in the range *(5.64)*. The resulting domain of C will be integers in the range *(3.62)*. For all three, this constrains the domain of residuals (i.e. errors) to integers in the range *(-59.59)*. For both threads of SHADE, errors will be distributed across these discrete value domains. For example, referring to Fig. 6, the probability of the center point difference being zero will be less than 0.4. In contrast, by configuring SHADE to only look for shadows of length greater than 33, the

Table 3 Effect of aircraft altitude on DEM-derived edge detection performance.

Altitude (MSL)	N	μ_{F^D}	μ_{B^D}	μ_{C^D}	σ_{F^D}	σ_{B^D}	σ_{C^D}
1600 m	12618	−0.01	0.00	−0.00	1.80	3.74	2.09
1800	17727	−0.26	−0.59	−0.41	3.34	5.04	3.58
2000	11813	0.04	−0.18	−0.11	1.72	4.77	2.52
2200	7028	−0.14	−0.05	−0.10	2.20	2.51	1.64
2400	4890	0.21	−0.06	0.04	1.66	2.12	1.43

integer domain changes to *(-29.29)*, effectively narrowing the distribution such that the probability of the center point difference being zero will increase significantly (i.e. the standard deviation decreases). As mentioned previously, the compromise here is that in certain operational environments we may not see enough long shadows. This will result in a loss of availability.

C. Shadow Feature Detection and Extraction Performance

Figures 7 and 8 illustrate the shadow environment, as perceived by SHADE, for two sample scans recorded on the DC-8 and G-V, respectively. The DC-8 scans (Fig. 7) occurred during the low level flight discussed previously near Modesto, CA. The G-V scans (Fig. 8) occurred on final approach to runway 16R at RNO. Radar altitude (RA), or height above the ground, is given on the figures for each scan. For the WxR-based plots, yellow indicates the range bins whose values are greater than zero and black indicates range bins whose values are zero, as measured by the radar. For the DEM-based plots, yellow indicates range bins that SHADE has determined are not shadowed and black indicates range bins that SHADE has perceived as shadowed. The sample scan data covers the area from $-45°$ to $+45°$ of azimuth in front of the aircraft flight path. Table 4 lists the respective WxR configurations.

The two scans shown in Fig. 7 occurred during a shallow climb with terrain clearance greater than 800 ft. Terrain signature can be characterized as moderate. In Scan 23, long shadows are seen by both threads of SHADE beyond 10 nmi in front of, and to the left, of the flight path. This shadowing effect is caused by rising terrain up to, and above, the aircraft altitude. This shadowing effect is again observed in Scan 25 beyond 8 nmi. The large feature in Scan 23 centered at 12 nmi and to the right of the flight path is the face of rising terrain that reflects most of the radar energy back to the source. The DEM-derived thread of SHADE observes this feature in both scans as well.

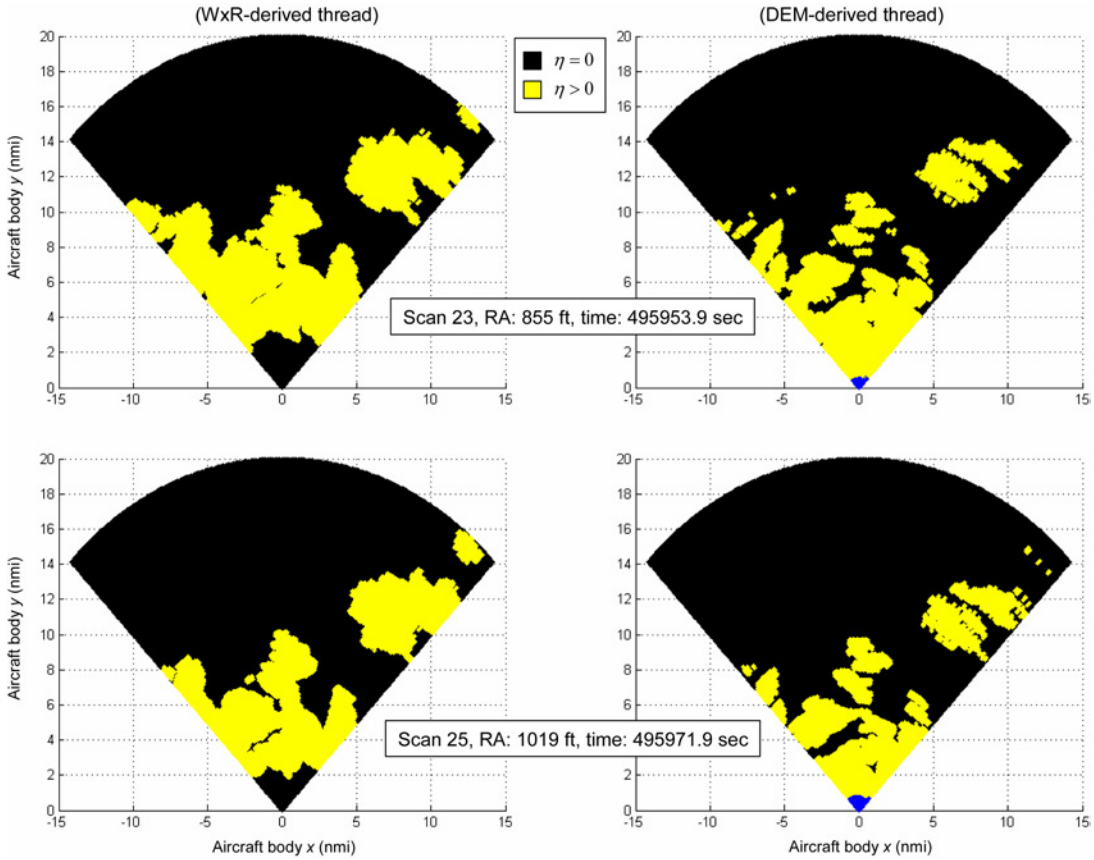

Fig. 7 SHADE results for scans from DC-8 testing.

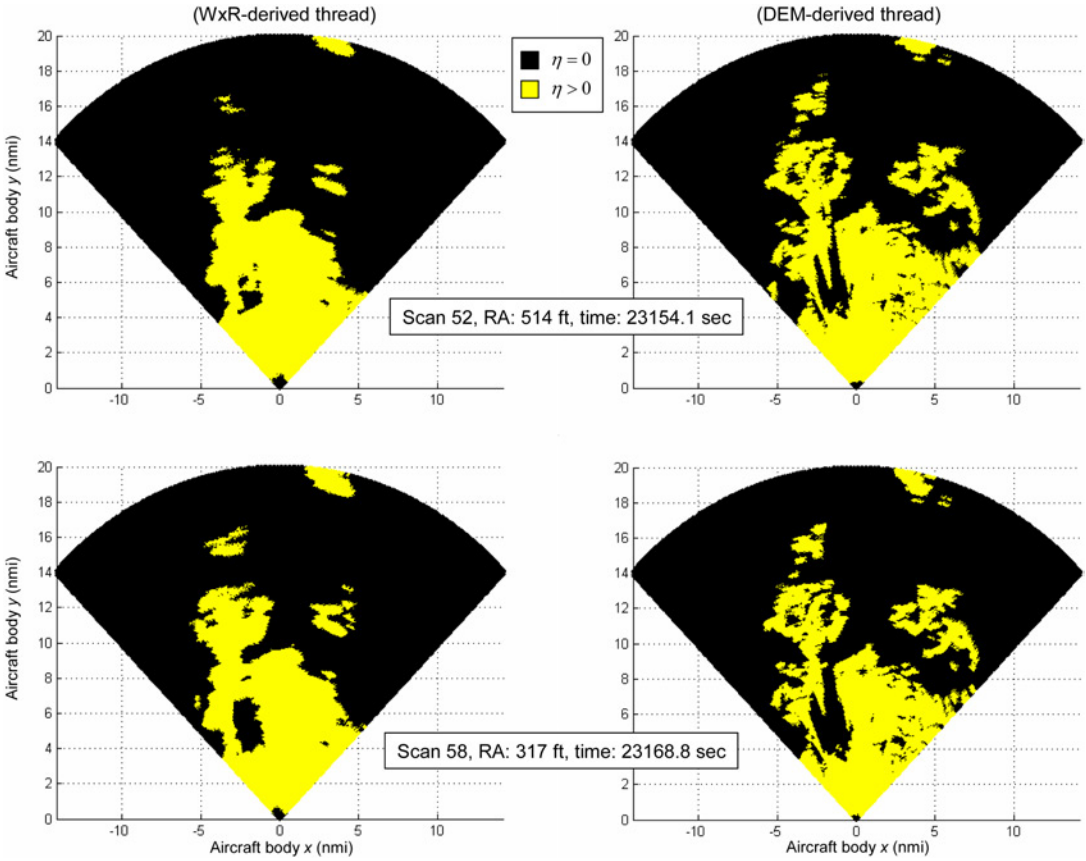

Fig. 8 SHADE results for scans from G-V testing.

The two scans shown in Fig. 8 occurred on final approach to runway 16R at RNO. Terrain signature can be characterized as moderate. As with the previous data set, terrain shadowing effects are apparent. A unique feature of interest is the shadow centered at 5 nmi in scan 52, just to the left of the flight path. This shadow is caused by Rattlesnake Mountain. This mountain is less than 1/4 mile from the far end of runway 16R and slightly left of runway heading. The elevation of Rattlesnake Mountain is 5,011 ft MSL, or ∼600 ft above the runway elevation. This is a significant visual reference for pilots operating at RNO. The shadow created by this mountain is apparent in both scans and in both threads of SHADE.

Table 4 WxR test configurations.

Parameter	DC-8	G-V
R	20 nmi	20 nmi
ΔR	144.8 m	144.8 m
M	256	256
σ^W	0.63	0.63
$\Delta\alpha$ (mean)	0.45°	0.25°
Δt (mean)	10.9 ms	6.5 ms
N (mean)	198/scan	376/scan
t_{scan} (mean)	2.2 sec	2.4 sec

D. Disparity and Bias Detection Performance

Figure 9 shows segments of representative approach trajectories flown by the G-V at RNO. Three-minute segments consisting of ∼60 scans, or ∼20,000 radial measurements, are used in this section to illustrate disparity and bias detection performance. For the approach segments, features output by the two threads of SHADE are down-sampled using a dynamic size constraint. This is based on an assumption that shadows should generally grow as the aircraft descends. From the previous discussion, we know that the uncertainty will be smaller for larger shadows and for shadows that are closer in range. Dynamic down-sampling logic was chosen to maintain an update rate greater than 10 Hz.

Figure 10 represents concatenated observations from segments of six straight-in approaches to runway 16R at RNO. The computed mean and standard deviation of disparity for these segments is consistent with the predicted performance derived from the calibration testing flown over the Modesto region with the DC-8. There are three factors contributing to the off-Normal appearance of the distribution. First, the logic chosen for constraining shadow size as the aircraft descends results in periods where neither thread detects a shadow. When neither thread sees a shadow, disparity is assigned zero. Ideally, the size constraint logic should minimize these periods. The second issue relates to periods during which the aircraft is changing heading. This heading change can be observed in Fig. 9 during the Sparks North approach procedure. Degraded performance, while turning, is most likely due to the latency of measurements coming from the radar and imperfect antenna stabilization. The third factor is the off-Normal distribution of errors

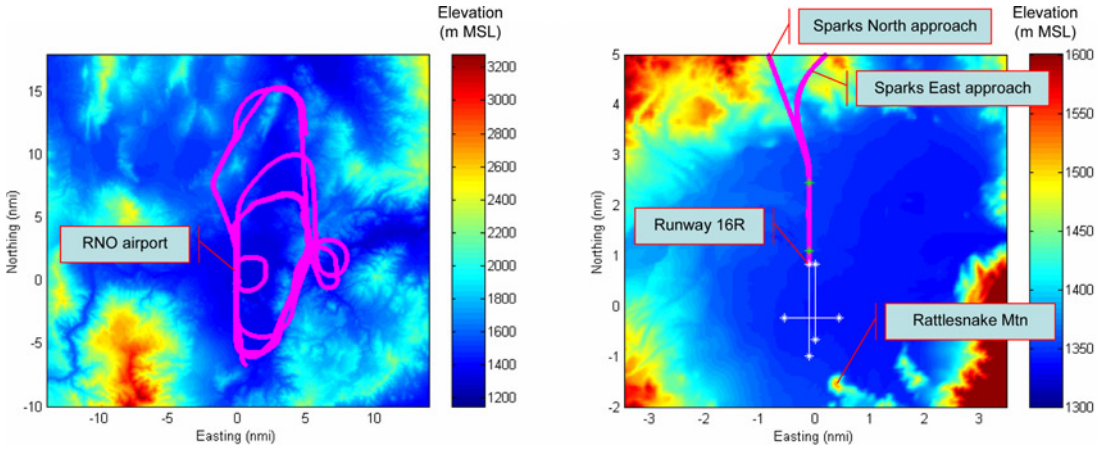

Fig. 9 Representative G-V trajectories at RNO.

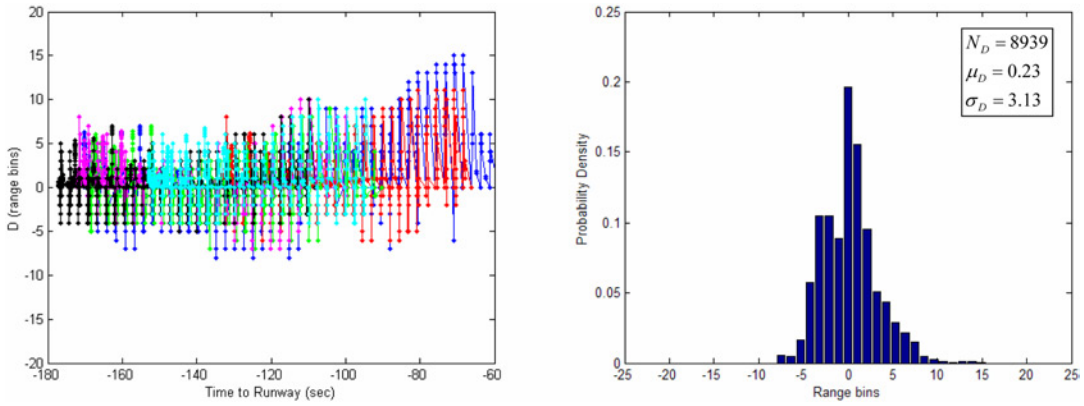

Fig. 10 Aggregate disparities during RNO approaches.

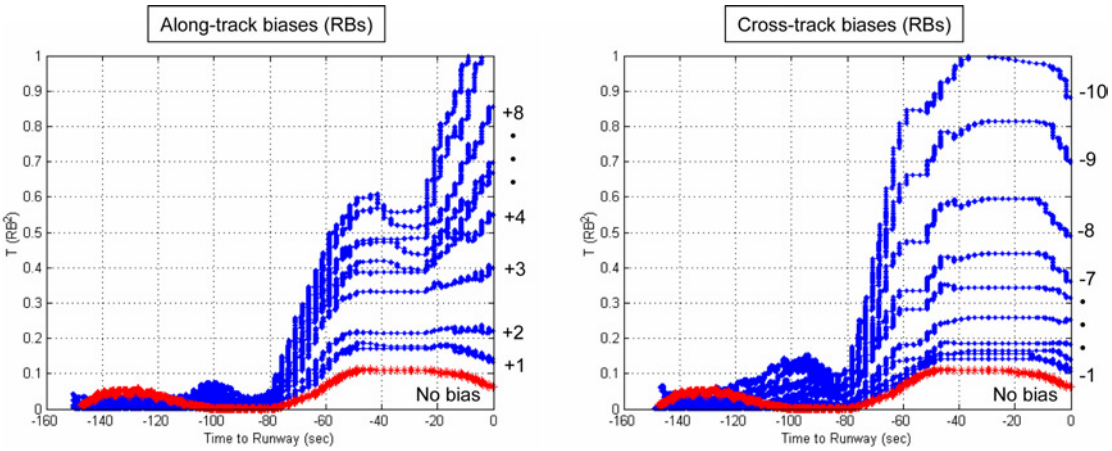

Fig. 11 T-values in the presence of bias errors.

for the shadow center points produced by both threads. This was observed during the calibration testing with the DC-8 and is re-enforced here.

Next, an example configuration was established to compute T using (11) for one of the RNO approach segments. R is set at 10 nmi and a fault-free value for σ_D is set at 5.66 range bins. This value results from using (9), with both σ_{C^D} and σ_{C^W} equal to four range bins. N_D is set to 720. This is approximately equal to the number of radial measurements in two scans from $-45°$ to $+45°$ at 0.25° spacing.

To verify our hypothesized detection capability, errors are inserted in the form of position biases (i.e. translations). Results are shown in Fig. 11 for one of the G-V approaches. As expected, for the zero bias case, T remains relatively small—less than 0.12; however, for the bias cases, T increases as more disparities are observed. The larger the bias, the sooner T exceeds the no-bias curve. For the cases shown in Fig. 11, setting the detection threshold at 0.12 would result in detection for all of the cross-track and along-track bias cases down to and including one range bin.

Consider that the selection of the detection threshold will have a direct effect on the probability of false alarm as illustrated by (17). Specifically, to detect all of the bias cases shown in Fig. 11, a threshold of 0.12 could be chosen; however, this may lead to a high false alarm probability that may be operationally unacceptable.

Note. The earlier discussion suggested a false alarm probability of 0.10 would yield a detection threshold of 2.71 using (17). Recall, this value was for detection of disparity bias. The positioning biases inserted in this section do not translate directly into a disparity bias but also affect the variance and distribution of disparities. The relationship between false alarm rate and detection threshold in the presence of positioning biases is to be determined.

VII. Summary and Conclusions

This article is motivated by a perceived need by the industry to quantify the integrity of terrain models that are to be referenced by pilots during low-level flight in low-visibility conditions. In operational environments where steering decisions are based on the proximity of terrain and proximity can only be estimated from a stored terrain model, system integrity must be assured. Remote sensing can provide this integrity either through monitoring or through an appropriate DEM update procedure.

The use of existing certified X-band radar technology is attractive as these radars are currently installed on many aircraft. A ground-mapping mode of operation is available that has been used historically by pilots to obtain a visual indication of terrain signature on a radar-specific display. This study introduces a method of extracting terrain features from the raw measurements and characterizing them with respect to features extracted from the stored DEM. Shadowing effects, caused by loss of line-of-sight by the radar, are used as the features of interest as they occur frequently during low-level flight operations. These are directly observable by the radar and can be extracted as the radar antenna scans. Independently, synthetic radial measurements are generated by the proposed algorithm, SHADE. SHADE makes use of (i) GPS positioning information, (ii) IRU attitude information, (iii) the radar antenna pointing angle, (iv) an antenna beam model, and (v) the DEM to estimate terrain shadowing from the airborne observer

during flight. Consistency, or disparity, checking is accomplished based on a statistical approach and elements of detection theory. A test statistic is proposed that enables errors to be detected with bounded probabilities of false alarm and missed detection.

Test results quantify the expected error distributions for features detected in a fault-free state using a calibration procedure. For the test equipment and DEM, shadow feature center point accuracies of 1.04 to 3.01 range bins and 1.43 to 3.58 range bins were found for the WxR- and DEM-derived threads of SHADE, respectively. This corresponds to 1.77 range bins to 4.68 range bins for the expected disparity in the fault-free state.

Shadow feature detection performance is demonstrated by test data acquired during a series of flights in Reno, NV. Measured disparity during these flights agrees with those derived from the calibration effort. The detection of DEM position biases as small as one range bin is verified for a WxR-2100 radar having a range bin size of 144.8 m. Detection capability should scale with improved range resolution.

In conclusion, while the proposed method shows promise, there are several issues that remain open. These have been identified and are the focus of continuing investigation.

Acknowledgments

The authors would like to thank the flight crew and engineers from NASA Dryden Flight Research Center and Gulfstream who supported the test aircraft that were used in this study. Jonathon Sayre's efforts developing the WxR data collection software and hardware is also very much appreciated. The work presented was supported, in part, through the NASA Langley Research Center under Cooperative Agreement NCC-1-351.

References

[1]Wehner, D. R., *High-Resolution Radar*, 2nd ed., Artech House, Norwood, MA, 1995.

[2]*Global Positioning System: Theory and Applications*, edited by B. W. Parkinson and J. J. Spilker, Jr., Vol. 163 and 164, Progress in Astronautics and Aeronautics, AIAA, Washington, DC, 1996.

[3]Titterton, D. H., and Weston, J. L., *Strapdown Inertial Navigation Technology*, Institution of Electrical Engineers Radar, Sonar, Navigation and Avionics Series 5, Peter Peregrinus, Ltd., on behalf of Institution of Electrical Engineers, Stevenage, UK, 1997.

[4]*Terrain Analysis: Principles and Applications*, edited by J. P. Wilson, and J. C. Gallant, Wiley and Sons, 2000.

[5]"Terrain Awareness and Warning Systems," United States Federal Register—Rules and Regulations, Federal Register Document 00-7595, Vol. 65, No. 61, pp. 16735–16756, March 27, 2000.

[6]Takallu, M., Wong, D., Bartolone, A., Hughes, M., and Glaab, L., "Interaction Between Various Terrain Portrayals and Guidance/Tunnel Symbology Concepts for General Aviation Synthetic Vision Displays During a Low En-route Scenario," *Proceedings of the 23rd AIAA/IEEE Digital Avionics Systems Conference*, AIAA/IEEE, Salt Lake City, UT, October, 2004.

[7]"User Requirements for Terrain and Obstacle Data," Document DO-276, RTCA, Washington, DC, March 5, 2002.

[8]"Performance Specification for Digital Terrain Elevation Data (DTED™)", United States Defense Mapping Agency, MIL-PRF-89020A, April 19, 1996.

[9]"Airborne Weather Radar with Forward-Looking Windshear Detection Capability," Airlines Electronic Engineering Committee, ARINC Characteristic 708-A-3, ARINC, Inc., November, 1999.

[10]Dieffenbach, O., "APALS™ Autonomous Precision Approach and Landing System," *Proceedings of the 9th Annual Symposium on Aerospace/Defense Sensing, Simulation, and Controls, Society of Photo-Optical Instrumentation Engineers (SPIE)*, SPIE, Orlando, FL, April, 1995.

[11]Morici, M., "Aircraft Position Validation using Radar and Digital Terrain Elevation Database", U. S. Patent Number 6,233,522, U. S. Patent Office, May 15, 2001.

[12]"WxR-2100 Multi-Scan Weather Radar", Data Sheet 523-780587-00111J 3M-AT-7/00-CS, Rockwell Collins, Cedar Rapids, IA, 2002.

[13]"Minimum Operational Performance Standards for Airborne Weather Radar with Forward-Looking Windshear Detection Capability", RTCA Document DO-220, RTCA, September 21, 1993.

[14]Ammar, D., Spires, R., and Sweet, S., "Radar Based Terrain and Obstacle Alerting Function", U. S. Patent Number 5,945,926, U. S. Patent Office, August 31, 1999.

[15]Gray, R. A., "In-flight Detection of Errors for Enhanced Aircraft Flight Safety and Vertical Accuracy Improvement Using Digital Terrain Elevation Data with an Inertial Navigation System, Global Positioning System and Radar Altimeter," Ph.D. Dissertation, Ohio University, Athens, Ohio, June 1999.

[16]Uijt de Haag, M., Campbell, J., and Gray, R., A terrain database integrity monitor for synthetic vision systems, AIAA/IEEE, *19th Digital Avionics Systems Conference*, October 7–13, 2000.

[17]Uijt de Haag, M., Sayre, J., Campbell, J., Young, S., and Gray, R., "Flight Test Results of a Synthetic Vision Elevation Database Integrity Monitor," *15th Annual International Symposium on Aerospace/Defense Sensing, Simulation, and Controls (AeroSense)*, SPIE, Orlando, FL, April 16–20, 2001.

[18]Young, S., Uijt de Haag, M., and Sayre, J., "Using X-band Weather Radar Measurements to Monitor the Integrity of Digital Elevation Models for Synthetic Vision," *Proceedings of the International Society for Optical Engineering (SPIE)—Enhanced and Synthetic Vision 2003*, edited by J. G. Verly, Vol. 5081, SPIE, Bellingham, WA, 2003, pp. 66–76.

[19]Young, S., Uijt de Haag, M., and Campbell, J., "An X-band Radar Terrain Feature Detection Method for Low Altitude SVS Operations and Calibration Using LiDAR," *Proceedings of the International Society for Optical Engineering (SPIE)—Enhanced and Synthetic Vision 2004*, edited by J. G. Verly, Vol. 5424, SPIE, Bellingham, WA, 2004, pp. 110–124.

[20]Young, S., Kakarlapudi, K., and Uijt de Haag, M., "A Shadow Detection and Extraction Algorithm using Digital Elevation Models and X-band Weather Radar Measurements," *International Journal of Remote Sensing*, Vol. 26, No. 8, 20 April 2005, pp. 1131–1149.

[21]Leon-Garcia, A., *Probability and Random Processes for Electrical Engineering*, 2nd ed., Addison-Wesley, Reading, MA, 1994.

[22]Scott, W., "NASA Team Brings Synthetic Vision to Maturity", *Aviation Week and Space Technology*, August 9, 2004, p. 48.

[23]Billingsley, J. B., *Low-Angle Radar Land Clutter Measurements and Empirical Models*, William Andrew Publishing, New York, NY, 2002.

[24]Skolnik, M. L., *Introduction to Radar Systems*, 2nd ed., McGraw-Hill, New York, NY, 1980.

[25]Long, M. W., *Radar Reflectivity of Land and Sea*, 3rd ed., Artech House, Boston, MA, 2001.

[26]http://www.optech.on.ca, cited Aug. 2005.

[27]Campbell, J., Uijt de Haag, M., Vadlamani, A., and Young, S., "The Application of LiDAR to Synthetic Vision System Integrity," *Proceedings of the 22nd AIAA/IEEE Digital Avionics Systems Conference*, AIAA/IEEE, Indianapolis, IN, October, 2003.

[28]http://www.ngs.noaa.gov/CORS/cors-data.html, cited Aug. 2005.

[29]http://www.applanix.com/html/products/prod_pac_index.html, cited Aug. 2005.

[30]Sayim, I., Pervan, B., Pullen, S., and Enge, P., "Experimental and Theoretical Results on the LAAS Sigma Overbound," *Proceedings of the Institute of Navigation GPS/GNSS Conference*, Portland, OR, September 24–27, 2002.